Analysis of Stress Wave Interaction with a 180° Bend Junction Between Two Square Bars

Salil Bavdekar[1,2], Joaquin S A Garcia[3], Amith A Cheenady[4], Andres Bernardo[2], Ghatu Subhash[2,*]

[1]Department of Mechanical Engineering, Illinois State University, Normal, IL, USA

[2]Mechanical and Aerospace Engineering Department, University of Florida, Gainesville, FL, USA

[3]Civil Engineering Institute, École Politechnique Fédérale de Lausanne, Lausanne, Switzerland

[4]Department of Materials Design and Innovation, University at Buffalo, Buffalo, NY, USA

*Corresponding author (subhash@ufl.edu)

Abstract

An analytical model for wave propagation through an unrestrained 180° bend junction connecting two long bars of rectangular cross-section is developed and the results are validated using experimental and numerical analyses. Upon arrival of a longitudinal stress wave, the bend junction is assumed to undergo rigid translation followed by rotation. By analyzing the normal and shear forces as well as the bending moments acting at the intersection of the bend junction, a set of 15 equations consisting of fifteen variables has been derived. Solving the system of equations in Laplace domain leads to transfer functions that relate the incident pulse to reflected and transmitted wave characteristics, as well as to the translation and rotation of the bend junction. These results in Laplace domain are converted back to time domain using the convolution integral. Concurrently, finite element analysis and experimental validation of the bend junction behavior were carried out to verify the results obtained from the analytical model. In addition to revealing the influence of individual parameters explicitly, the model revealed that the efficiency of the unrestrained bend junction for transmission of the longitudinal waves is at most ∼70% for a long duration stress pulse. This limitation is a result of the rotation of the bend junction which emanates flexural waves into both the bars. Thus, further increase in transmission efficiency of longitudinal wave is possible if the bend junction is restrained to move only in the axial direction with no rotation.

Keywords: wave mechanics, wave propagation, waveguide, transfer function, DIC

1. Introduction

One-dimensional elastic stress wave propagation through a straight bar has been well studied for almost eighty years (Bancroft, 1941; Chree, 1886; Morse, 1948; Pochhammer, 1876; Rayleigh, 1945, 1888). Since the 1970s, wave propagation phenomenon through junctions between two straight bars connected at various angles has been investigated both analytically and experimentally (Atkins and Hunter, 1975; Guo et al., 2010; Lee and Kolsky, 1972; Maurel et al., 2014; Subhash et al., 2026, 2022; Yong and Atkins, 1983, 1982). Of particular interest is the longitudinal stress wave interaction with a 90° bend junction connecting two bars (Atkins and Hunter, 1975; Lee and Kolsky, 1972; Yong and Atkins, 1983, 1982). When a longitudinal stress pulse was passed into the first (input) section of the bar, Lee and Kolsky (1972), remarked that "It is perhaps surprising that when $\theta = 90°$, a small longitudinal pulse is still propagated along the second (output) section of the bar". This longitudinal wave in the output bar was in addition to the expected flexural wave. Recent analysis by Subhash et al. (2022) revealed that upon the arrival of the longitudinal wave, the 90° bend junction initially translates in the direction of the wave propagation thus generating a flexural wave in the output bar; followed by junction rotation, generating a longitudinal wave in the output bar. When a similar analysis was extended to a 180° bend junction restricted to only axial motion, shown schematically in Fig. 1(a), a complete transmission of the longitudinal stress wave with reversal in sign was noted in the output bar; i.e., a compression stress wave in the input bar emerged as a tensile stress wave in the output bar without loss in its amplitude and duration. Based on 1-dimensional analysis, the transfer function H for this behavior was derived in the Laplace domain as

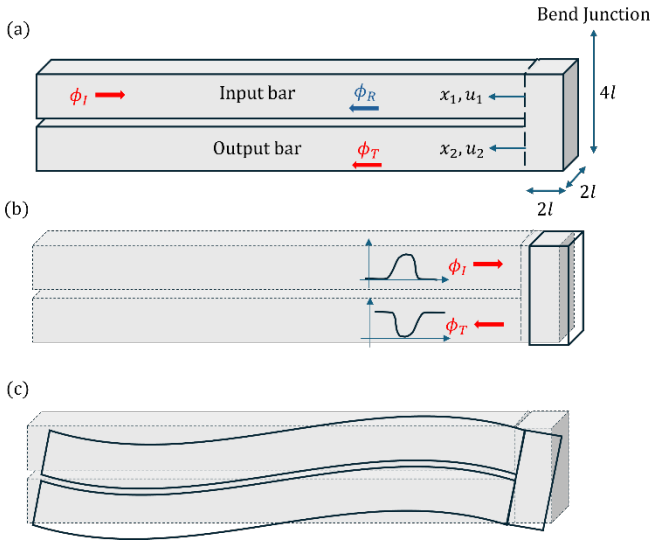

Fig. 1. (a) Schematic of the 180° bend junction. (b) Translation followed by (c) rotation of the junction upon arrival of the stress wave.

$$H_{1D}(s) = \frac{\hat{\phi}_T(s)}{\hat{\phi}_I(s)} = \frac{1}{1 + \frac{2l}{c}s} = \frac{1}{1 + T_{ch}s} \tag{1}$$

where $\hat{\phi}_I$ and $\hat{\phi}_T$ are the incident and transmitted waves, respectively, in Laplace space ($\hat{\phi}(s) = \mathrm{L}[\phi(t)]$). Here, L stands for the Laplace transform and s is the Laplace frequency. T_{ch} is the characteristic time, defined as the time required for the longitudinal elastic wave (with velocity c) to traverse the junction of dimension $2l$ (see Fig.1(a)).

Eq. (1) can be inverted back to time domain as

$$\phi_T(t) = -\int_0^t \frac{\exp(-\tau/T_{ch})}{T_{ch}} \phi_I(t-\tau)d\tau \tag{2}$$

which can be interpreted as an exponential kernel in a convolution integral. In Eqs. (1) and (2), the longitudinal waves may be represented in terms of displacement or axial stress; the only difference

is that the transfer function for stress is opposite in sign ($H_{\sigma_T} = -H_{\phi_T}$), as the incident compressive wave in the input bar is transmitted as a tensile wave in the output bar.

It is noted from Eq. (1) that the junction behaves as a low pass filter, and most of the incident wave is transmitted through the junction when the duration of the incident stress pulse is significantly longer than T_{ch} (Subhash et al., 2022). This result was achieved because the junction initially translates in the direction of wave motion upon the arrival of the compressive stress wave as shown schematically in Fig. 1(b), pulling the output bar to generate a tensile longitudinal wave in it. Based on this mechanistic understanding, Subhash et al. proposed a "millipede bar" concept that can be used to propagate long-duration longitudinal stress pulses through several rods joined together alternatingly at 180° bend junctions in a serpentine fashion to form a continuous wave guide (Subhash et al., 2026). These results were validated both experimentally and through numerical simulations of the junction behavior (Subhash et al., 2026, 2022). However, although the junction was constrained laterally, it was found that the junction translates unevenly between the input and output bar segments as the amplitude of the incident longitudinal wave increases. This results in the twisting of the junction, leading to bending of the input and output bars as schematically illustrated in Fig. 1(c). This bending introduces flexural waves into both the bars. Thus, long after the longitudinal wave is generated in the output bar, flexural waves are also induced in both the bars.

The analytical solution proposed by Subhash et al. (2022) employs a one-dimensional formulation for the bars and assumes an axially constrained rigid junction. While this 1D model was able to predict the long duration longitudinal wave propagation behavior correctly, it was incapable of capturing the characteristics of the flexural waves, especially when the incident stress wave was of shorter duration. To date, no analytical formulation exists to describe or predict these

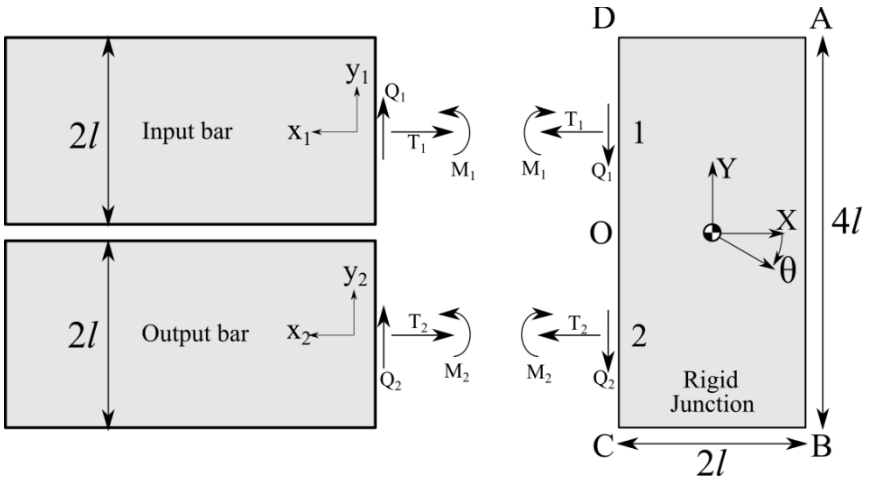

Fig. 2. Free body diagram of the 180° bend junction and the associated forces and moments at the intersection of the junction with rods. The points at the bar-junction interface along the centerline of the input and output bars are indicated by 1 and 2, respectively. The corner points of the junction are indicated by A, B, C, and D, and the junction "tip" is indicated by O.

phenomena. In this article, we derive a two-dimensional analytical model for the behavior of an unconstrained 180° bend junction when a longitudinal wave arrives at the junction from the input bar, and validate these results through finite element simulations and experimental measurements.

2. Analytical model for wave propagation through an unrestricted 180^{o} bend junction

A schematic of the 180° bend junction connecting two bars with rectangular cross-sections was shown in Fig. 1(a). The incident longitudinal wave (ϕ_I) arrives at the junction through the input bar and is partially transmitted (ϕ_T) into the output bar and partially reflected (ϕ_R) back into the input bar. Upon arrival of the stress wave, the bend junction translates and then twists as shown in Figs. 1(b) and 1(c), respectively (Subhash et al., 2022). To analyze this behavior, the normal and

shear forces T_1 and T_2, Q_1 and Q_2, respectively, and bending moments M_1 and M_2 acting at the intersection of the bend junction and the input and the output bars are shown in Fig. 2. The subscripts 1 and 2 are used to denote the quantities acting on the input and output bars, respectively. The free-body diagrams in Fig. 2 also illustrate the local coordinate systems for the bars (x_i, v_i) and the junction (X, Y). The rigid body translation and rotation of the junction will be captured in the analytical model in terms of horizontal and vertical movement of the corner points A–D. The junction "tip", denoted by point O, lies on the bar-junction interface, equidistant between C and D. The objective of this model is to derive various transfer functions for translation and rotation of the junction as well as the magnitudes of reflected and transmitted waves in terms of the incident wave characteristics.

In a previous study, Subhash et al. (2022) developed a 1D model which considered only axial motion (U) of the bend junction and neglected the lateral degrees of freedom. In the current effort, motivated by the solutions of Atkins and Hunter (1975), the junction is still modeled as a rigid body, but its lateral movement *(V)* and rotation *(θ)* will be considered along with the vertical deflections *(v_1, v_2)* of both input and output bars. The cross-sections of the bars are modeled as squares with an area $2l \times 2l$, and the junction has a width of $2l$, a depth $2l$, and a height $4l$ (see Fig. 2). The separation between the two bars is assumed negligible. Thus, the total mass m of the junction is $16\rho l^3$, where ρ is the density of the bar material.

In the following, a bar on a symbol implies it has physical units and a symbol without a bar refers to its dimensionless counterpart. An arrow (→) indicates a transition from physical definition to the dimensionless form. The horizontal and vertical displacement fields in the rigid junction are defined as $\overline{u}(x, y, t)$ and $\overline{v}(x, y, t)$, respectively. We nondimensionalize the spatial and temporal variables as $\xi = x/l$, $\eta = y/l$, and $\tau = t/(l/c)$, where c is the wave velocity in the bar

material. We can rewrite the corresponding displacement fields as $\Phi u(\xi,\eta,\tau)$ and $\Phi v(\xi,\eta,\tau)$, where $\Phi = \phi/\overline{\phi}$ is the characteristic amplitude of the input wave. Similarly, the movement of the center of mass of the junction is defined by horizontal displacement $\overline{U}$, vertical displacement $\overline{V}$, and rotation $\overline{\theta}$ (assuming small rotation $\overline{\theta} \ll 1$). Then the relation between the motion of center of mass of the junction and that of the input bar can be given by

$$\overline{u}(Y,t) = \overline{U} + \mathrm{Y}\overline{\theta} \rightarrow u(\eta,\tau) = U + \eta\theta \tag{3a}$$

$$\overline{v}(X,t) = \overline{V} - \mathrm{X}\overline{\theta} \rightarrow u(\xi,\tau) = V - \xi\theta \tag{3b}$$

where $\theta = \overline{\theta}/(\Phi/l)$, $\eta \in [-2,2]$, $\xi \in [-1,1]$ based on dimensions of the junction (see Fig. 2).

The incident longitudinal wave $\overline{\phi}_I(x_1 + ct) = \Phi\phi_I(\xi_1 + \tau)$ is partially transmitted as $\overline{\phi}_T(x_2 - ct) = \Phi\phi_T(\xi_2 - \tau)$ to the output bar and the rest is reflected back into the input bar as $\overline{\phi}_R(x_1 - ct) = \Phi\phi_R(\xi_1 - \tau)$. The displacement fields u and v, along the centerline of the input bar at the bar-junction interface (point 1 in Fig. 2), can now be related to the rigid junction as

$$\overline{u}_1(x_1 = 0, y_1 = 0, t) = \overline{u}(Y = l, t) = \overline{U} + l\overline{\theta} \rightarrow u_1(\xi_1 = -1, \eta_1 = 1, \tau) = U + \theta \tag{4a}$$

$$\overline{v}_1(x_1 = 0, y_1 = 0, t) = \overline{v}(X = -l, t) = \overline{V} + l\overline{\theta} \rightarrow v_1(\xi_1 = -1, \eta_1 = 1, \tau) = V + \theta \tag{4b}$$

Similarly, for the output bar (at point 2 in Fig. 2)

$$u_2(\xi_2 = -1, \eta_2 = -1, \tau) = U - \theta \tag{5a}$$

$$v_2(\xi_2 = -1, \eta_2 = -1, \tau) = V + \theta \tag{5b}$$

The continuity of horizontal displacements between the rigid junction and the bar implies that

$$\phi_I(\xi_1 = -1, \tau) + \phi_R(\xi_1 = -1, \tau) = u_1(\xi_1 = -1, \eta_1 = 1, \tau) = U + \theta \tag{6a}$$

$$\phi_T(\xi_2 = -1, \tau) = u_2(\xi_2 = -1, \eta_2 = -1, \tau) = U - \theta \tag{6b}$$

From Eqs. (4) and (5), it is seen that while the horizontal displacements of the input and output bars are different (i.e., $U + \theta$ and $U - \theta$), the vertical displacements are the same ($V + \theta$). This will give rise to the same vertical displacement of both the bars and hence, the flexural deflections of both the bars occur in unison, as shown in Fig. 1(c). This result is in agreement with finite element simulations performed during the previous study by Subhash et al. (2022) for a constrained junction.

Consistent with the Euler-Bernoulli beam theory (i.e., assuming small deflections with planar cross-sectional areas remaining planar and normal to the neutral axis during bending of the rods), the slope of the rods should be equal in magnitude to the rotation θ of the rigid junction. Hence, the derivatives of the vertical displacement are given by

$$\left.\frac{\partial v_1}{\partial \xi_1}\right|_{\xi_1=0} = \theta \tag{7a}$$

$$\left.\frac{\partial v_2}{\partial \xi_2}\right|_{\xi_2=0} = \theta \tag{7b}$$

The axial strains at the joint between the rods and the bend junction are given by

$$\bar{\epsilon_1} = \frac{\partial \bar{u}_1}{\partial x_1} \rightarrow \epsilon_1 = \frac{\epsilon_1}{\Phi/l} = \frac{\partial u_1}{\partial \xi_1} \tag{8a}$$

$$\bar{\epsilon_2} = \frac{\partial \bar{u}_2}{\partial x_2} \rightarrow \epsilon_2 = \frac{\epsilon_2}{\Phi/l} = \frac{\partial u_2}{\partial \xi_2} \tag{8b}$$

Similarly, the corresponding axial forces are

$$\bar{T}_1 = E_1 A_1 \bar{\epsilon_1} \rightarrow T_1 = \frac{\bar{T}_1}{E_1 A_1 \Phi/l} \rightarrow T_1 = \epsilon_1 = \left.\frac{\partial(\phi_I + \phi_R)}{\partial \xi_1}\right|_{\xi_1=0} = \phi_I'(\tau) - \phi_R'(\tau) \tag{9a}$$

$$\bar{T}_2 = E_2 A_2 \bar{\epsilon_2} \rightarrow T_2 = \frac{\bar{T}_2}{E_2 A_2 \Phi/l} \rightarrow T_2 = \epsilon_2 = \left.\frac{\partial \phi_T}{\partial \xi_2}\right|_{\xi_2=0} = -\phi_T'(\tau) \tag{9b}$$

Note that T is equal to ϵ in dimensionless form only.

The bending moments and shear forces (see Fig. 2) for the input and output bars can be written as

$$\bar{M}_i = E_i \mathcal{I}_i \frac{\partial \bar{\theta}_i}{\partial x_i} \rightarrow M_i = \frac{\bar{M}_i}{A_i \Phi} \rightarrow M_i = \left(\frac{\mathcal{I}_i}{A_i l^2}\right) \frac{\partial \theta_i}{\partial \xi_i} = \frac{1}{3} \frac{\partial^2 v_i}{\partial \xi_i^2} \tag{10}$$

for $i = 1, 2$; and

$$\bar{Q}_i = \frac{\partial \bar{M}_i}{\partial x_i} \rightarrow Q_i = \frac{\bar{Q}_i}{E_i A_i \Phi / l} \rightarrow Q_i = \frac{\partial M_i}{\partial \xi_i} \tag{11}$$

for $i = 1, 2$. Here, the second moment of the cross-section area $\mathcal{I}$ of a square section of side $2l$ (with respect to its center) is $\mathcal{I} = (4/3)l^4 = Al^2/3$, where A $(= 4l^2)$ is the cross-sectional area of the input bar or output bar. The equations of equilibrium for the junction can now be written from the free-body diagram (Fig. 2) as

$$T_1 + T_2 = -\frac{\partial^2 U}{\partial \tau^2} \tag{12a}$$

$$Q_1 + Q_2 = -\frac{\partial^2 V}{\partial \tau^2} \tag{12b}$$

$$(T_1 - T_2) - (Q_1 + Q_2) + (M_1 + M_2) = \frac{20}{3} \frac{\partial^2 \theta}{\partial \tau^2} \tag{12c}$$

The above equations for moment and shear forces can be combined to derive the Euler-Bernoulli equation for flexural waves as

$$\frac{\partial^4 \bar{v}_i}{\partial x_i^4} + \left(\frac{\rho_L}{E\mathcal{J}}\right) \frac{\partial^2 \bar{v}_i}{\partial t^2} = 0 \rightarrow \frac{\partial^4 v_i}{\partial \xi_i^4} + 3 \frac{\partial^2 v_i}{\partial \tau^2} = 0 \tag{13}$$

2.1. Solution for the Flexural Equation

To obtain the complete solution for the 2D model, we solve Eq. (13) by applying Laplace transforms quiescent initial conditions, i.e.,

$$\frac{d^4\hat{v}_i}{d\xi_i^4} + 3s^2\hat{v}_i = 0 \tag{14}$$

There are two possible solutions that decay as $\xi_i \to \infty$. Hence,

$$\hat{v}_i(\xi_i, \tau) = \alpha_i(s) \exp\left(-(1+i)\xi_i\sqrt{\sqrt{3}s/2}\right) + \beta_i(s) \exp\left(-(1-i)\xi_i\sqrt{\sqrt{3}s/2}\right) \tag{15}$$

So, instead of solving for $\hat{v}_i$, we can solve for the coefficients α_i and β_i. The following relations emerge in Laplace domain.

From Eqs. (3) and (4) for v_i, we get

$$\alpha_1 + \beta_1 = \hat{V} + \hat{\theta} \tag{16a}$$

$$\alpha_2 + \beta_2 = \hat{V} + \hat{\theta} \tag{16b}$$

From Eqs. (7) and (15),

$$\alpha_1\left(-(1+i)\xi_i\sqrt{\frac{\sqrt{3}s}{2}}\right) + \beta_1\left(-(1-i)\xi_i\sqrt{\frac{\sqrt{3}s}{2}}\right) = \hat{\theta} \tag{17a}$$

$$\alpha_2\left(-(1+i)\xi_i\sqrt{\sqrt{3}s/2}\right) + \beta_2\left(-(1-i)\xi_i\sqrt{\sqrt{3}s/2}\right) = \hat{\theta} \tag{17b}$$

From Eqs. (10) and (15),

$$\alpha_1\left(-(1+i)\xi_i\sqrt{\frac{\sqrt{3}s}{2}}\right)^2 + \beta_1\left(-(1-i)\xi_i\sqrt{\frac{\sqrt{3}s}{2}}\right)^2 = 3\hat{M}_1 \tag{18a}$$

$$\alpha_2\left(-(1+i)\xi_i\sqrt{\frac{\sqrt{3}s}{2}}\right)^2 + \beta_2\left(-(1-i)\xi_i\sqrt{\frac{\sqrt{3}s}{2}}\right)^2 = 3\hat{M}_2 \tag{18b}$$

From Eqs. (11) and (18),

$$\alpha_1\left(-(1+i)\xi_i\sqrt{\frac{\sqrt{3}s}{2}}\right)^3+\beta_1\left(-(1-i)\xi_i\sqrt{\frac{\sqrt{3}s}{2}}\right)^3=3\hat{Q}_1 \tag{19a}$$

$$\alpha_2\left(-(1+i)\xi_i\sqrt{\frac{\sqrt{3}s}{2}}\right)^3+\beta_2\left(-(1-i)\xi_i\sqrt{\frac{\sqrt{3}s}{2}}\right)^3=3\hat{Q}_2 \tag{19b}$$

Thus, the problem now contains fifteen equations consisting of the two relations between wave amplitudes and horizontal displacements from Eqs. (6), the two constitutive relations for axial force from Eqs. (9), the three equilibrium equations from Eqs. (12), the two relations between α and β for vertical displacements from Eqs. (16), the two relations between α and β for the rotation from Eqs. (17), the two relations between α and β for bending moments from Eqs. (18), and the two relations between α and β for shear forces in Eqs. (19). The relevant fifteen unknowns are the three rigid-body junction motions: $\hat{U}$, $\hat{V}$, and $\hat{\theta}$; the four forces and two moments acting over junction: $\hat{T}_1, \hat{T}_2, \hat{Q}_1, \hat{Q}_2, \hat{M}_1, \hat{M}_2$; the four coefficients: $\alpha_1, \alpha_2, \beta_1, \beta_2$; and the two amplitudes of longitudinal waves: $\hat{\phi}_T$ and $\hat{\phi}_R$ (we assume the input pulse $\hat{\phi}_I$ is known *a priori* or measured in an experiment).

These fifteeen equations in Laplace domain are solved as a system of algebraic equations with fifteen unknowns using Wolfram Mathematica. The solution is derived in terms of the known variable $\hat{\phi}_I(s)$. The result for any variable divided by $\hat{\phi}_I(s)$, yields the transfer function for the said variable. The previous 1D model [9] resulted in a simple transfer function (Eq. (1)) that could be inverted back to time domain analytically (Eq. (2)) once the input pulse $\phi_I(t)$ and thus $\hat{\phi}_I(s)$ was defined. Unfortunately, such is not the case in this 2D model. The equations, though manageable in closed form, do not lend themselves to inversion readily. So, instead of using the convolution integral to obtain the time evolution of transmitted signals readily, we resort to

numerical inversion of the closed-form expressions, in Laplace domain, for the relevant times. Such computations can be readily performed in Wolfram Mathematica (or Python), to obtain the stress wave transmitted to the output bar and reflected in the input bar, the horizontal and vertical movement of the four corners of the junction, and the rotation of the junction, all as a function of the input stress amplitude. These results will be shown along with the numerical results in Section 4, after discussing these models in more detail. Note that s is a dimensionless Laplace frequency and to get physical values, we substitute $s \rightarrow \bar{s}l/c$. The corresponding transfer functions for various relevant parameters are given below.

Input axial displacement to junction horizontal movement

$$H_U(s) = \frac{\hat{\mathrm{U}}}{\hat{\phi}_I} = \frac{1}{(1+2s)} \tag{20}$$

Input axial displacement to junction vertical movement

$$\begin{aligned} H_U(s) &= \frac{\hat{\mathrm{V}}}{\hat{\phi}_I} \\ &= \frac{\sqrt[4]{3}\left(\sqrt{2}3^{3/4} + 6\sqrt{s}\right)}{20\sqrt{3}s^2 + 16\sqrt{2}\sqrt[4]{3}s^{\frac{3}{2}} + 6\sqrt{3}s + 12s + 2\sqrt{2}3^{\frac{3}{4}}\sqrt{s} + 3\sqrt{2}\sqrt[4]{3}\sqrt{s} + \sqrt{3}} \end{aligned} \tag{21}$$

Input axial displacement to junction rotation

$$\begin{aligned} H_\theta(s) &= \frac{\hat{\theta}}{\hat{\phi}_I} \\ &= -\frac{3\sqrt{2}\sqrt[4]{3}\left(\sqrt{2}\sqrt[4]{3}\sqrt{s} + 1\right)\sqrt{s}}{20\sqrt{3}s^2 + 16\sqrt{2}\sqrt[4]{3}s^{\frac{3}{2}} + 6\sqrt{3}s + 12s + 2\sqrt{2}3^{\frac{3}{4}}\sqrt{s} + 3\sqrt{2}\sqrt[4]{3}\sqrt{s} + \sqrt{3}} \end{aligned} \tag{22}$$

The incident and transmitted axial stress amplitudes can be calculated as $\hat{\sigma}_I(s) = \rho c s \hat{\phi}_I$ and $\hat{\sigma}_T(s) = \rho c s \hat{\phi}_T$, respectively (Subhash et al., 2022). Recalling that $H_{\sigma_T} = -H_{\phi_T}$, we can write

$\hat{\sigma}_T(s) = H_\sigma(s)\hat{\sigma}_I(s) = -H_\phi(s)\rho cs\hat{\phi}_I$. The corresponding transfer functions for the stress waves are thus given below.

Input axial stress to transmitted axial stress

$$H_{\sigma_T}(s) = -\frac{\hat{\sigma}_T}{\hat{\sigma}_I} = \frac{\hat{\phi}_T}{\hat{\phi}_I}$$
$$= -\frac{8\sqrt{3}s^2 + 10\sqrt{2}\sqrt[4]{3}s^{3/2} + 12s + 2\sqrt{2}3^{3/4}\sqrt{s} + \sqrt{3}}{(2s+1)(20\sqrt{3}s^2 + 16\sqrt{2}\sqrt[4]{3}s^{\frac{3}{2}} + 6\sqrt{3}s + 12s + 2\sqrt{2}3^{\frac{3}{4}}\sqrt{s} + 3\sqrt{2}\sqrt[4]{3}\sqrt{s} + \sqrt{3})} \quad (23)$$

Input axial stress to reflected axial stress

$$H_{\sigma_R}(s) = -\frac{\hat{\sigma}_R}{\hat{\sigma}_I} = \frac{\hat{\phi}_R}{\hat{\phi}_I}$$
$$= -\frac{40\sqrt{3}s^3 + 32\sqrt{2}\sqrt[4]{3}s^{5/2} + 24s + 4\sqrt{2}3^{3/4}s^{3/2} - 4\sqrt{3}s - 3\sqrt{2}\sqrt[4]{3}\sqrt{s}}{(2s+1)(20\sqrt{3}s^2 + 16\sqrt{2}\sqrt[4]{3}s^{\frac{3}{2}} + 6\sqrt{3}s + 12s + 2\sqrt{2}3^{\frac{3}{4}}\sqrt{s} + 3\sqrt{2}\sqrt[4]{3}\sqrt{s} + \sqrt{3})} \quad (24)$$

The flexural wave amplitude can be determined as half the difference in axial stress amplitudes at the extreme points at any cross-section on the input or output bars. At the bar-junction interface on the output bar, these extreme points are $\mathrm{C}(X = -l, Y = 2l \rightarrow \xi_2 = -1, \eta_2 = -2)$ and $\mathrm{O}(X = -l, Y = 0 \rightarrow \xi_2 = -1, \eta_2 = 0)$. At these points,

$$\hat{\phi}_T(\mathrm{C}) = \hat{\phi}_T(\xi_2 = -1, \eta_2 = -2) = u_2(\xi_2 = -1, \eta_2 = -2) = \hat{U} - 2\hat{\theta} \quad (25a)$$

$$\hat{\phi}_T(\mathrm{O}) = \hat{\phi}_T(\xi_2 = -1, \eta_2 = 0) = u_2(\xi_2 = -1, \eta_2 = 0) = \hat{U} \quad (25b)$$

Hence, the flexural wave in the output bar,

$$\hat{\sigma}_{\text{flex}} = \left|\frac{\hat{\sigma}_T(\mathrm{C}) - \hat{\sigma}_T(\mathrm{O})}{2}\right| = \left|\frac{-\rho cs\left[\hat{\phi}_T(\mathrm{C}) - \hat{\phi}_T(\mathrm{O})\right]}{2}\right| \quad (26)$$

From Eqs. (25) and (26),

$$\hat{\sigma}_{\text{flex}} = \left| \frac{-\rho cs\left[\hat{U} - 2\hat{\theta} - \hat{U}\right]}{2} \right| \tag{27}$$

Hence,

$$\hat{\sigma}_{\text{flex}}(s) = \left| \rho cs\hat{\theta} \right| \tag{28a}$$

$$\hat{\sigma}_{\text{flex}}(s) = \left| \rho csH_{\theta}(s)\hat{\phi}_I \right| \tag{28b}$$

Due to rigid junction assumption and the symmetry of the problem, Eq. (28) also applies to the flexural waves in the input bar, with only a change in sign. This implies that the flexural waves in both bars can be eliminated if the junction rotation is constrained, i.e., $\hat{\theta} = 0$.

In Section 4, we test the predictions obtained from inverting these transfer functions back to the time domain (using numerical inverse Laplace transform and then convolving with the input pulse in time domain) against FE simulations and experimental results in time domain.

2.2. Reduction to the 1D Model

It can be shown that this 2D model reduces to the 1D formulation if lateral displacements are constrained. From Eq. (20),

$$\hat{U} = \frac{\hat{\phi}_I}{(1 + 2\text{s})} \tag{29}$$

Substituting Eq. (29) into the Laplace transform of Eq. (6b),

$$\hat{\phi}_T = \hat{U} - \hat{\theta} = \frac{\hat{\phi}_I}{(1 + 2\text{s})} - \hat{\theta} \tag{30}$$

Recall that all solutions so far are in dimensionless quantities. To revert to physical values, we substitute $s \rightarrow \bar{s}l/c$ and $\theta = \overline{\theta}/(\Phi/l)$, to get

$$\hat{\phi}_T = \frac{\hat{\phi}_I}{\left(1 + \frac{2l}{c}s\right)} - l\hat{\theta} \tag{31}$$

In terms of the transfer functions given in Eqs. (1), (22), and (23),

$$\hat{\phi}_T = H_{1\mathrm{D}}(s)\hat{\phi}_I - l\hat{\theta} \tag{32a}$$

$$H_{\sigma_T}(s) = \frac{\hat{\phi}_T}{\hat{\phi}_I} = H_{1\mathrm{D}}(s) - lH_\theta(s) \tag{32b}$$

If the junction is laterally constrained so that only axial displacement is allowed, i.e., $\theta = 0$, Eq. (32) reduces to the 1D formulation given in Eq. (1). This implies that the junction rotation (θ) decreases the magnitude of the longitudinal stress wave transmitted into the output bar.

3. Numerical and Experimental Methods

The assumptions and performance of the 2D model presented in the previous section are compared to numerical results obtained from finite element simulations, as well as experimental results obtained with high-speed imaging and digital image correlation.

3.1. Finite Element Model Setup

Two-dimensional (plane-stress) finite element (FE) simulations were conducted using ABAQUS/CAE 2024. The FE model comprised two 300 mm long bars of 4 mm × 4 mm square cross-section that were connected to a junction of length 4 mm ($2l$) and height 8 mm ($4l$). The bars, which are identified as 'Input bar' and 'Output bar' in Fig. 3(a), are separated by a gap of 0.1mm and unconstrained in the lateral directions. A total of 243,240 CPS4R 4-node elements of size 0.1 mm were used to discretize the model and the explicit FE simulations were run at a fixed

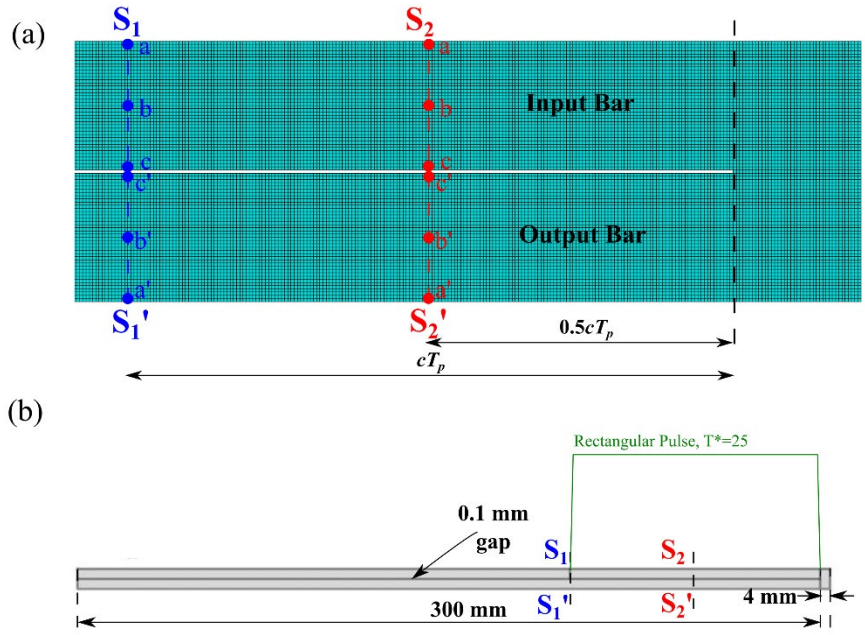

Fig. 3. (a) Discretized FE model showing the locations of the cross-sections where stress amplitudes were measured during wave propagation. (b) A schematic of the bars showing the incident rectangular pulse dimensions relative to the junction dimension.

time increment of 0.01 μs. The bars were assigned a Young's modulus, E = 200 GPa, Poisson's ratio, ν = 0.26, and density, ρ = 7850 kg/m^3. The longitudinal wave velocity in the bar is thus given by $c = \sqrt{E/\rho}$ = 5047.5 m/s.

A longitudinal stress pulse of duration T_p = 19.55 μs is generated by pushing the part of the input bar behind S1 (see Fig. 3(a)) against the rest of the bar with a velocity loading function $v(t) = V_0\, \varphi_I(t)$ m/s, where $\varphi_I(t)$ represents a unit rectangular pulse and $0 \leq t \leq 19.55$ μs. Note that this pulse duration is about 25 times the duration for the stress wave to transfer through the bend junction (i.e., $T^* = 25$), as indicated in Fig. 3(b). The amplitude of the incident stress wave is dependent on the impact velocity of the striker. However, all the elements in the problem are linear (linear elastic material response and assumed small deformations); hence, regardless of the stress amplitude and the bar dimensions, the trends in the results remain the same. In this study, two

values of V_0, 1.187 m/s and 10.1 m/s (corresponding to 47 MPa and 400 MPa of axial stress, respectively), were employed. The lower value (V_0 = 1.187 m/s, σ_0 = 47 MPa) was chosen to match the experimental input stress (to be discussed in the next section). The higher value (V_0 = 10.1 m/s, σ_0 = 400 MPa) was chosen for illustrative purposes because the bend junction behavior can be better visualized and rationalized due to the larger displacements and resolution.

The generated pulse propagates through the input bar and interacts with the unconstrained 180° bend junction, resulting in a portion of the input wave being reflected back into the input bar while the rest is transmitted into the output bar. The stress amplitudes of the waves were measured at four cross-sections (identified as S_1, S_2, S_2', and S_1') along the bars, as shown in Fig. 3. S_1 and S_2 are located on the input bar at distances cT_p and $0.5cT_p$, respectively, from the junction. S_1', and S_2' are similarly located on the output bar. These locations were chosen to avoid stress concentration effects due to the sharp edges at the bend junction and to minimize interference with the waves reflecting off the junction. The longitudinal and flexural waves in both bars were quantified using axial stresses measured at three points (a, b, c and a', b', c') across every cross-section as shown in Fig. 3(a). The longitudinal wave amplitude was calculated along the centerline of the bars (e.g., b at section S_1 in Fig. 3(a)) and the flexural wave amplitude was calculated as half the difference in stress amplitudes at the extreme points (e.g., a and c at section S_1) at every cross-section.

3.2. Experimental Setup

The experimental setup, shown in Fig. 4(a), is similar to that in the authors' previous work (Subhash et al., 2022). However, the previous work only measured the incident, reflected, and

transmitted axial waves using strain gages. In this work, we measure the bend junction displacement and rotation using digital image correlation (DIC).

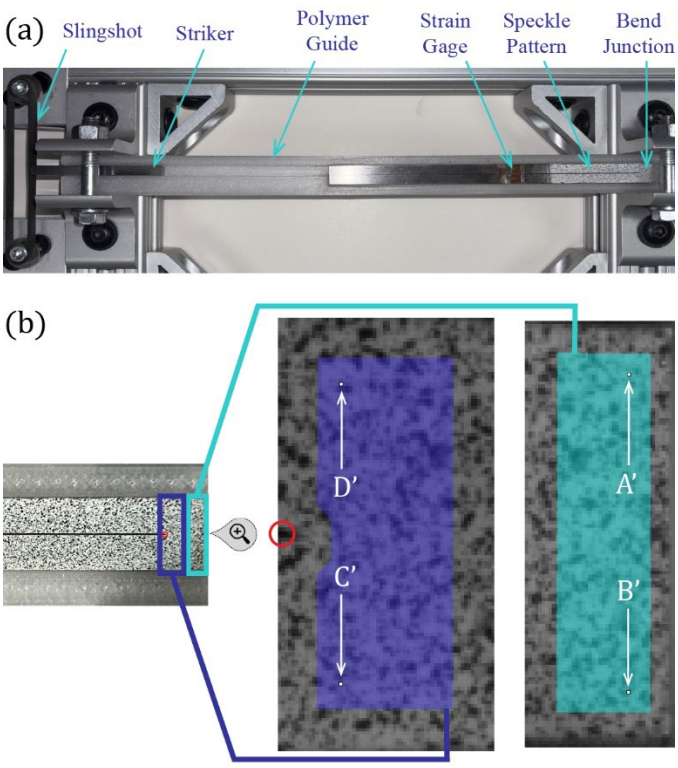

Fig. 4. (a) Experimental setup for DIC analysis of bend junction deformation. (b) Locations of measurement for corner displacement. The junction tip is circled in red.

The input and output bars are fabricated from an initial bar (A36 low-carbon steel) measuring 155 mm x 5 mm x 10 mm wide. A slot 250 μm wide is cut along the center of the bar via wire electric discharge machining (EDM), resulting in two square bars with dimensions slightly less than 5 mm × 5 mm. The slot ends 5 mm from the edge of the bar on one side, thus creating the 180° bend junction, similar to those shown in Figs. 1-3. A striker with the same cross-sectional area was also fabricated from the same steel stock, with a length of 62.5 mm (to achieve $T^* = 25$), resulting in a pulse duration of ~25 μs. The bars and the striker were seated in a low-friction polymer guide fabricated from High Impact Polystyrene (Z-HIPS®). The experimental setup was fitted with a rubber band "slingshot" to launch the striker at ~1.2 m/s.

The entire experimental setup was rigidly held in another frame and then mounted on an optical table. The bend junction and a portion of the bar segments adjacent to the bend were speckled with spray paint for DIC analysis. A high-speed camera (Vision Research Phantom v710, Ametek Company, Wayne, New Jersey) was focused on the bend junction to capture the movement of the

speckle pattern during the stress wave propagation. The horizontal and vertical displacements (and by extension, rotation) of the bend junction were measured and averaged at four points near the corners ($X = \pm 1.3$ mm, $Y = \pm 3.6$ mm), shown in Fig. 4(b). Measurements for corners A′ and B′ were captured at a frame rate of 500,000 fps (2 μs/frame) with an image resolution of 128 px × 48 px, while measurements at corners C′ & D′ were captured at a frame rate of 397,600 fps (~2.5 μs/frame), for an image resolution of 128 px × 64 px. The frame rate was selected to capture enough data points in the region of interest for a total event duration of 75 μs.

Several challenges must be acknowledged when attempting to measure displacement in the junction using DIC. First, regardless of the striker velocity, the 180° bend junction experiences extremely small deformations compared to the deformations in the input and output bars. This is because the bend junction acts as a rigid body and transfers the input pulse into the output pulse first by translation and then rotation, to generate axial and flexural waves, respectively (Subhash et al., 2022). Second, due to finite memory on the high-speed camera, a high frame rate of 500,000 fps (used for the measurements at A′ and B′) limits the maximum image resolution to 128 px × 64 px. The lower frame rate (397,600 fps) for the measurements at C′ and D′ is to accommodate a larger viewing window and include the junction tip in the frame. Hence, strain gages were also mounted on both, the input and output, bars to obtain higher resolution signals and to verify the DIC results. Overall, the DIC measurement agreed well with the strain gage measurements, giving confidence in the experimental results.

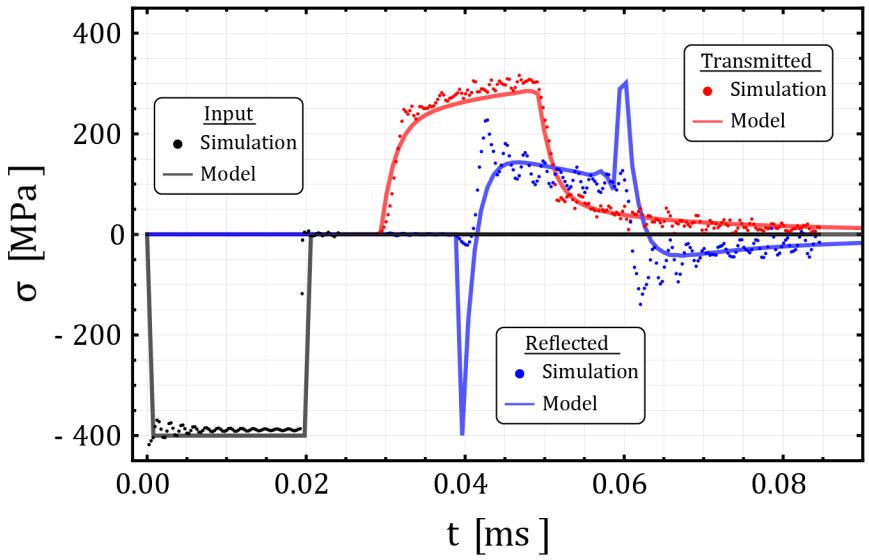

Fig. 5: Comparison of analytical model and finite element simulation results for the transmitted and reflected pulses.

4. Results and Discussion

Subhash et al. (2022) had previously established that laterally-constrained bend junction successfully transmits a longitudinal pulse, unaltered in magnitude and shape, when (i) the pulse duration (T_p) is significantly longer than the time needed for the wave to traverse the bend junction width (i.e., $T_p \gg T_{ch} = 2l/c$), and (ii) the pulse shape has a longer duration at its peak amplitudes (e.g., a square pulse compared to a triangular pulse). Therefore, in this work, we show results corresponding to a rectangular incident pulse, $\overline{\phi}_I$,with $T^* = T_p/T_{ch} = cT_p/2l = 25$.

4.1. Incident, Transmitted, and Reflected Pulses

The analytical and finite element (FE) simulation results for the transmitted and reflected pulses resulting from a rectangular input pulse of amplitude 400 MPa are shown in Fig. 5. Recall that in FE simulations, the input stress wave propagates through a short length of the bar before entering the junction (see Fig. 3(b)). The incident, reflected, and transmitted waves are measured at an equal

distance away from the junction. This length of the wave propagation introduces some dispersion and Pochhammer-Chree oscillations (Kolsky, 1964) into the wave in FE simulations. In the analytical model, the pulse is directly input into the bend junction and measured immediately after it emerges. The small amplitude differences in the input pulse and the reflected pulses seen in Fig. 5 are attributed to these dispersive effects. The output pulse has a peak magnitude less than 300 MPa, i.e., less than 75% of the input amplitude, and this peak occurs about 20 μs from the start, which is the end of the input pulse peak duration.

Thus, the unrestricted bend junction severely deteriorates the incident pulse in both its magnitude and duration. The analytical model compares well with the results of the FE simulations in both the transmitted and reflected signals. An interesting point to note is that there is about 10 μs delay in the reflected pulse compared to the transmitted pulse. This difference implies that there is a significant transient stress state within the bend junction, i.e., the junction first moves (translates) in the direction of wave travel on the input side and then drags the output side of the junction in the same direction after a gap of about 8 μs. This motion induces tensile stress in the output bar (transmitted pulse) as seen in Fig. 5. As time progresses, the continuous loading on the input side of the junction causes it to move more than the output side, thus causing a twist or rotation of the entire junction. As there is no lateral constraint on the bars and the junction, this twisting bends the two bars in unison as shown in Fig. 1(c), thus introducing flexural waves in the junction as well as some reflected pulse. Note that it was shown by Subhash et al. (Fig. 5 in Subhash et al. (2022)) that if the bend junction is restricted to axial motion only, the junction moves as a rigid bar and the transmitted pulse emerges immediately at the end of the input pulse duration with almost no reflected pulse.

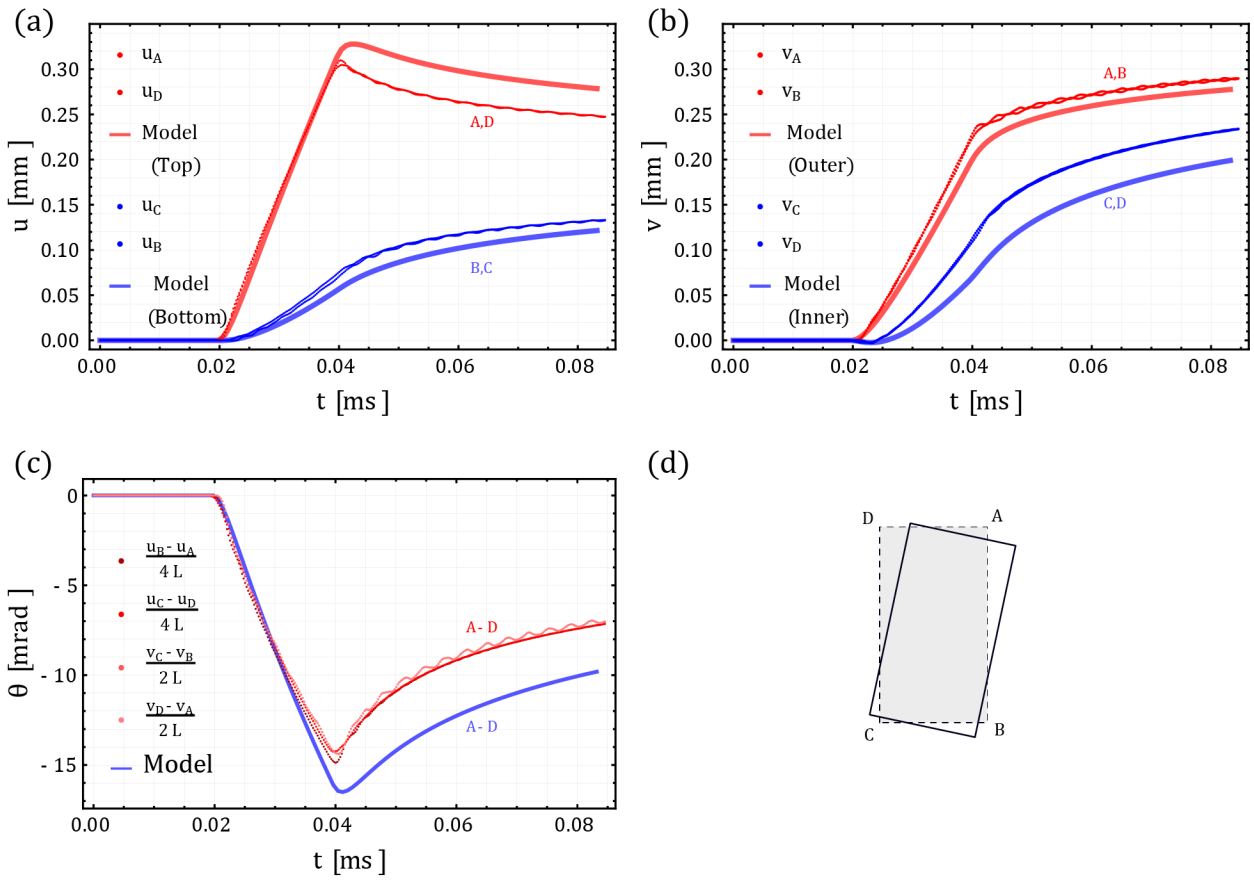

Fig. 6: Comparison of analytical model results and FE simulations for (a) horizontal movement and (b) vertical movement and (c) rotation of the junction at four corners. (d) Schematic of the junction rotation and corner points for reference.

4.2. Junction Deformation

The analytical and FE simulation results for the horizontal displacement (u), vertical displacement (v), and the rotation (θ) at the four corners of the bend junction are shown in Fig. 6. Recall that the bend junction is treated as a rigid body in the analytical solution but is a deformable body in the FE simulation. Hence, the amplitudes of u and v due to the analytical model depend on the movement of the center of mass (U, V) and rotation (θ) of the junction, as seen in Eq. (3). In Fig. 6, all three plots reveal an initial liner portion followed by a non-linear response. The linear

response extends over a duration of approximately 20 μs, corresponding to the input pulse duration; the non-linear portion corresponds to the unloading part.

Due to the rigid junction assumption, points A and D (top) will have the same values for horizontal displacement and points B and C (bottom) will have the same values but lower than the former two. This is because for both sets of points, the motion consists of a translation part (positive horizontal component) and a rotational part (twist) in the clockwise direction (see Fig. 6(d) for reference). For points A and D, the translational motion and the horizontal component of the rotation add and for points B and C, the latter subtracts from the former due to the clockwise rotation of the junction. Since all points show a positive value for horizontal displacement, the translation motion along the x-axis is larger than the horizontal component of the rotational part. Similar arguments can be made for vertical displacement. Here points A and B (outer) will have slightly higher values than points C and D (inner) due to the clockwise rotation of the junction. This is why there are only two plots for the analytical model in Figs. 6(a) and 6(b). Lastly, the rigid junction has the same value for θ at all four corners of the bend junction and hence, only one plot is required for the analytical model in Fig. 6(c). Overall, the trends of these motions in the analytical model match well with the FE simulations. Also, note that all FE simulation data reveal some waviness, and the period of these oscillations corresponds to the roundtrip travel time of wave reflections within the junction.

Interestingly, the top two corners (A and D) reach a peak value and then decrease slowly, indicating the relaxation (untwist) of the junction; however, the bottom two corner points (B and C) continue to increase slowly, indicating the delay due to inertia of the bottom section of the junction. On the other hand, the vertical displacement of all the corner points increases continuously even during the unloading portion. Recall that the position of the four corners depends on the rotation as well

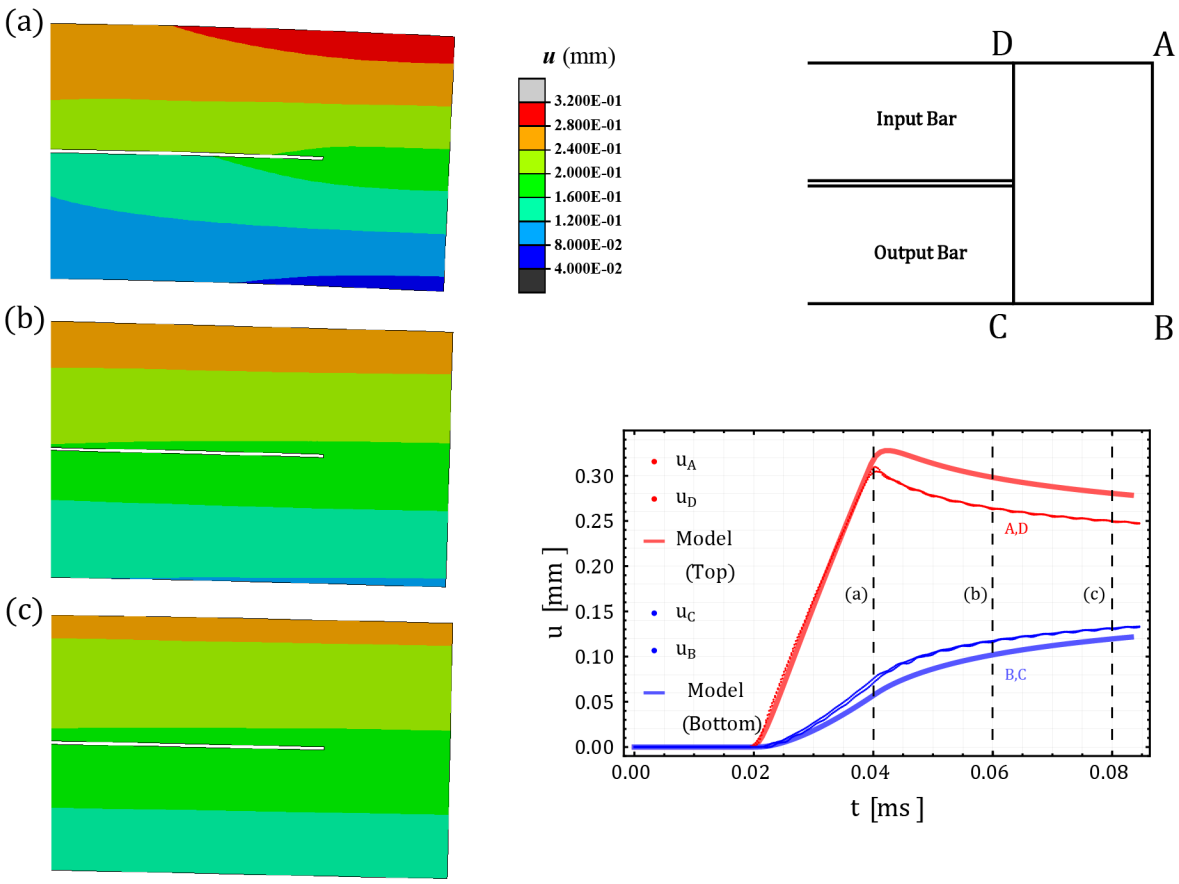

Fig. 7: Magnified images of the bend junction illustrating the horizontal displacement magnitudes (in mm) at times indicated in the graph on the right. Notable differences in magnitudes of horizontal displacements between the upper corner points and bottom corner points can be seen.

as the translation of the center of mass. Although rigid body assumption is still valid, the displacement amplitudes undergo a transient phase when the wave enters the junction and then settles over a long duration compared to the duration of the input pulse. The fact that some corners overshoot beyond a peak value of linear response and some others do not is due to this transient state. To better clarify these results, a sequence of deformation images corresponding to the transient time of the junction from the FE simulations are provided in Figs. 7 and 8. The color scale in these images reveals that the displacements of the top two corner points are not the same as those of the bottom two corner points. Note from the scale that these displacements are

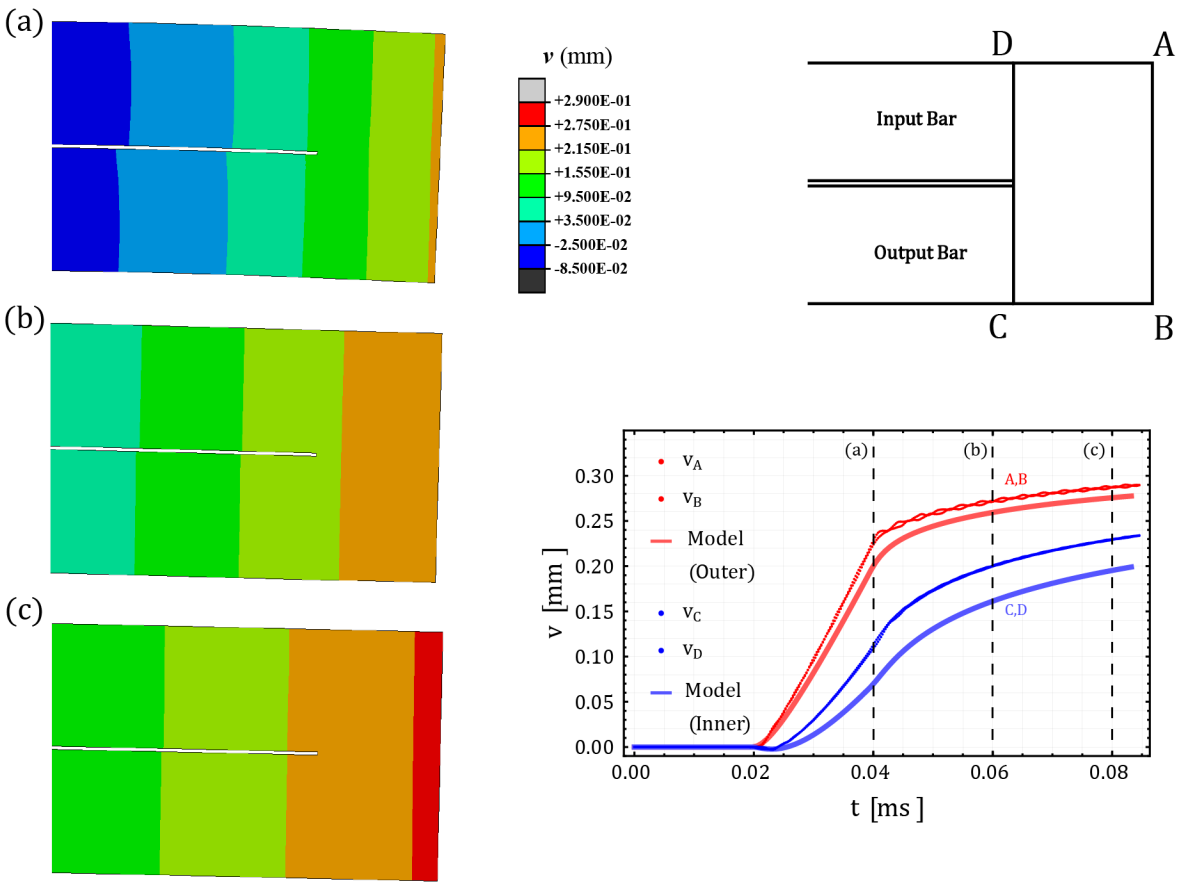

Fig. 8: Magnified images of the bend junction illustrating the vertical displacement magnitudes (in mm) at times indicated in the graph on the right. Notable differences in magnitudes of vertical displacements between the upper corner points and bottom corner points can be seen.

extremely small (on the order of couple of microns) for an input pulse magnitude of 400 MPa, which validates the assumption of rigid junction for most practical purposes.

The behavior of the junction rotation, Fig. 6(c), follows the same trend as the horizontal motion of the corners. The differences between the FE simulations and the analytical model results indicate that the assumption of rigid junction in the model is not strictly correct. The junction does undergo some level of elastic deformation which results in a maximum error of 15%. In addition to the

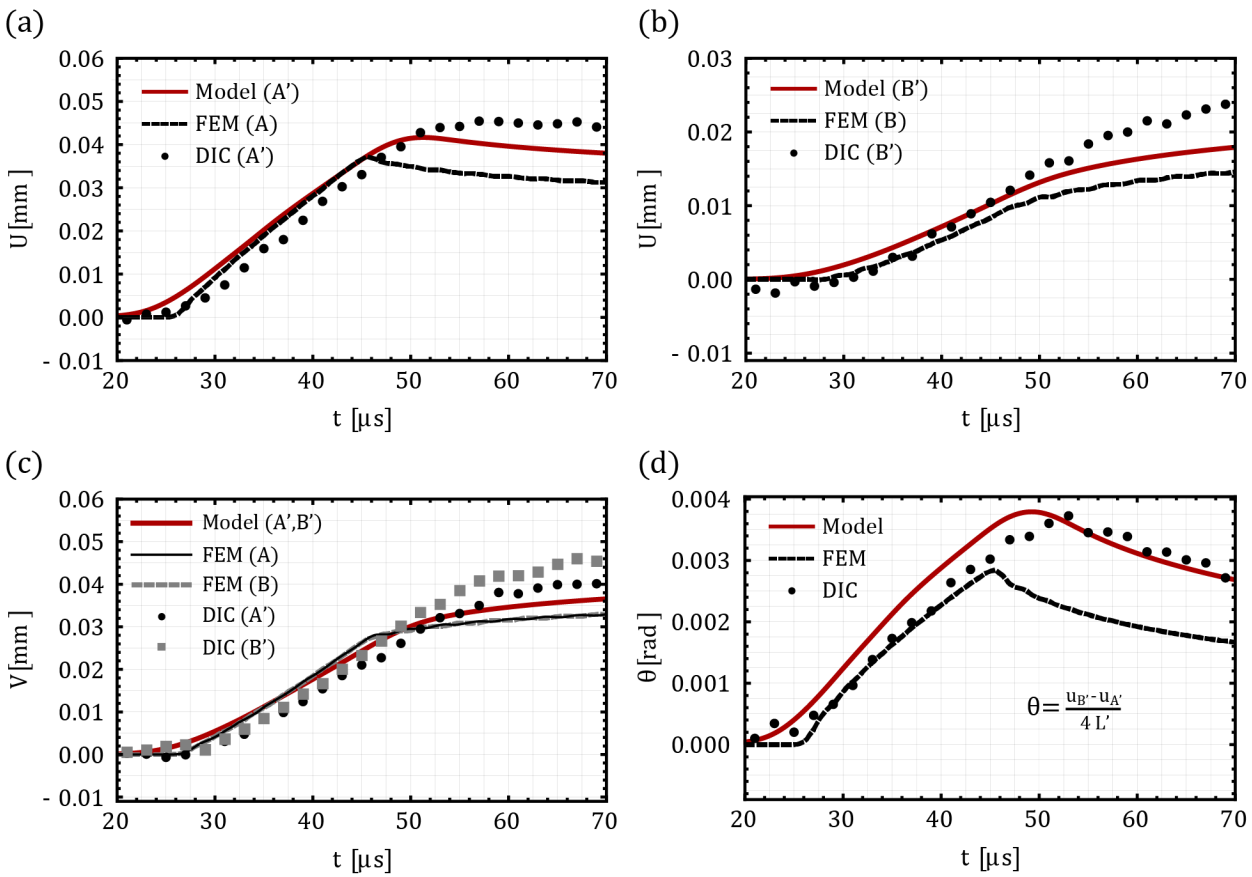

Fig. 9. Comparison of analytical model (red), finite element model (FEM), and experimental (DIC) results for (a) horizontal displacement near the top corner, (a) horizontal displacement near the bottom corner, (c) vertical displacement near both outer corners, and (d) rotation of the junction.

differences in rigid junction assumption, the amplitude difference in the input pulse (see Fig. 5) due to its dispersion-prone travel in the simulation also has some finite effect.

4.3. Experimental Validation

The analytical, numerical, and experimental results of the bend junction motion for an input pulse of amplitude 47 MPa are compared in Fig. 9. The analytical model and experimental (DIC) results are from the measurements at points near the corners but slightly in the interior (A', B', C', D' in Fig. 4(b)). The input pulse for the analytical model is obtained from strain gages attached to the

input bar, as shown in Fig. 4(a). In all these DIC measurements, the accuracy of the measurements depends on the density of speckle pattern and the size of the speckles, with higher density and smaller size speckles providing better results. At the same time, if a larger region is chosen for analysis in experiments, then comparison to a specific point in numerical analysis becomes less reliable. Therefore, one may only be able to compare the trends between the experimental and analytical/numerical results in a semi-quantitative fashion, rather than with exact values. In Fig. 9, the horizontal displacements for the top point A′ (Fig. 9(a)) as well as the bottom point B′ (Fig. 9(b)) match well in the trends as well as magnitudes in all three models. The vertical displacements at the outer points (A′ and B′) are plotted in Fig. 9(c). Due to the rigid-junction assumption in the analytical model, it predicts the same values for both points and hence, only one is shown. Finally, the measured rotation values are plotted in Fig. 9(d). The rotation of the junction is calculated using formulae similar to those shown in Fig. 6(c), but using only points near the outer corners. It is important to note that the FE analysis results for rotation are more conservative (stiffer) than analytical and experimental models. This is because in the analytical model, we assume rotation about one single point (point O in Fig. 2); however, in FE analysis the slot is 0.1 mm thick, and the junction rotates about a wider region. Furthermore, the numerical discretization also artificially stiffens the system a bit. Despite these differences, the overall agreement between the results is satisfactory as the analytical model predicts the experimental observations well. This result further validates the ability of the 2D model to correctly capture the deformation characteristics of the 180° bend junction.

4.4. Transfer Efficiency

The analytical model provides additional insight into the efficiency of the bend junction transfer characteristics. Here, we define “transfer efficiency” as the ratio between the output pulse peak

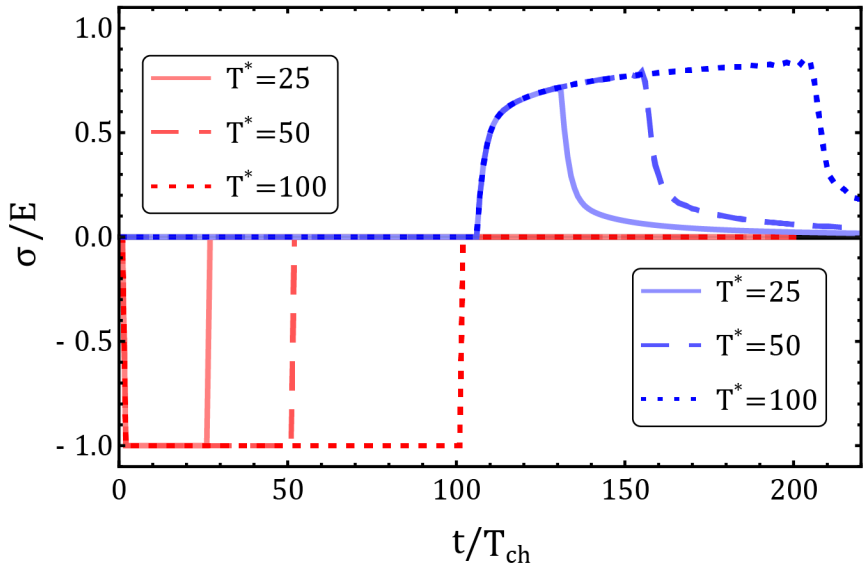

Fig. 10. Transfer efficiency of the bend junction for various durations of the incident stress pulse ($T^* = T_p/T_{ch}$). Even when T^* is increased by 4 times, the increase in efficiency is only ~13%.

amplitude to the input pulse peak amplitude. Comparing the transmitted pulse amplitude to the input pulse in Fig. 10, we note that the transfer efficiency of the unrestrained junction is at most ~72% for $T^* = 25$. This is a remarkable result considering that with no restriction on the movement of the bend junction, we can achieve such high efficiency. This result can be further improved if the T^* value is increased, but the increase in transfer efficiency is not significant. Even when T^* is increased by 4 times (i.e., from 25 to 100), the increase in efficiency is only 13% (i.e., from ~72% to ~85%). This result highlights that for peak performance of the bend junction, in addition to ensuring that $T^* \gg 1$, the vertical motion of the junction must be restrained. Results obtained earlier by Subhash et al. (2026, 2022) show that transfer efficiency up to 99% can be obtained under such conditions.

The model also provides insight into the question of why the transfer efficiency changes when the junction is not laterally constrained. From Eq. (31(a)), we can gather that the dimensionless transmitted displacement profile $\hat{\phi}_T$ is equal to that of the input $\hat{\phi}_I$ times the 1D transfer function

minus $l\hat{\theta}$. Hence, the presence of junction rotation term alters the transfer function and prevents full transmission of longitudinal pulse even when T^* is large. When the junction motion is constrained, i.e., $\hat{\theta} = 0$, we obtain the result of the 1D model. Of course, note from Eq. (22) that the rotation in turn also depends on the input pulse shape and amplitude, i.e., $\hat{\theta}(s) = H_\theta(s)\hat{\phi}_I(s)$. Previous publications (Subhash et al., 2026, 2022) have demonstrated that pulse shapes with longer peak amplitudes (e.g., rectangular and sinusoidal pulses) result in better transmission efficiency than pulse shapes with short or sharp peaks (e.g., triangular and Gaussian pulses). Finally, from Eq. (27), we note that the flexural waves result in both bars from the junction rotation $\hat{\theta}$. Hence, constraining the junction to prevent rotation can also eliminate these flexural waves.

The above fundamental knowledge about transfer efficiency can also guide us in our attempts at analyzing the efficacy of a "millipede bar" made of multiple rods connected via 180° bend junctions at alternate rod ends in a serpentine manner (Subhash et al., 2026). For a well-designed bar with multiple junctions, the transmitted pulse characteristics at the end of N number of bend junctions can be easily determined by simply raising the transfer function (Eqs. 20-24) by power N, as opposed to modeling the entire millipede bar in FE simulations. Our future efforts will focus on design and fabrication of a millipede bar with suitably designed end constraints to prevent bend junction rotation and evaluate its efficacy in transmitting a longitudinal wave unaltered over several bend junctions. Such waveguide designs will lay foundation for efficient as well as economical construction of novel test equipment such as drilling tools, piling columns, and split Hopkinson pressure bars with a shorter footprint.

5. Conclusions

A 2D analytical model was derived for the stress wave transfer characteristics through an unrestrained 180° bend junction by considering the forces and moments acting at the interface between the junction and the two connecting bars. Explicit transfer functions were derived for horizontal and vertical motion, rotation of the bend junction, and for reflected and transmitted wave amplitudes in terms of input pulse characteristics. The model captures the behavior of the bend junction effectively and compares well with the results of numerical simulations and experimental measurements. Upon arrival of the stress wave, the unrestricted bend junction first translates in the direction of the input wave and then rotates. Both the translation and rotational motions are linear with time, indicating the linear nature of deformation behavior of the unrestrained bend junction. Although the bend junction is considered rigid in the analytical model, the deviation of the model predictions from the FE and experimental results indicates that the bend junction does experience small elastic deformation.

The benefits of the analytical model are clear. The model considers the parameter influence explicitly and thus saves us from having to run FE simulations for every parameter combination. The FE model confirms that the assumptions made in our analytical model were valid. The 2D model reveals that the efficiency of the bend junction for transmission of an elastic longitudinal stress wave is about 72% when the pulse width is 25 times the characteristic length of the junction; however, this efficiency increases only marginally even when the pulse duration is increased by several folds. The model also predicts that when the bend rotation is eliminated, the junction efficiency increases to that of a laterally restricted bend junction, matching the 1D model result previously published by the authors (Subhash et al., 2026, 2022).

Declarations

Funding

This research was supported by the Army Research Office under grant no: W911NF2420192 with program manager Dr. Denise Ford.

Competing Interests

Ghatu Subhash has one patent active (Subhash and Whittington, 2025) and one patent pending (Subhash et al., Pending) for stress waveguides based on the 180° bend junction.

Code Availability

The code used to solve and plot the results of the analytical model is available at: https://github.com/SubhashUFlorida/millipede-bar

Author Contributions

Salil Bavdekar: Methodology, Formal Analysis, Investigation, Writing – Original Draft, Writing - Review & Editing. **Joaquin S A Garcia:** Methodology, Software, Formal Analysis, Writing – Original Draft, Visualization. **Amith A Cheenady:** Methodology, Software, Writing – Review & Editing, Visualization. **Andres Bernardo:** Validation. **Ghatu Subhash:** Conceptualization, Resources, Writing – Original Draft, Supervision, Project Administration, Funding Acquisition.

References

Atkins, K.J., Hunter, S.C., 1975. The propagation of longitudinal elastic waves around right-angled corners in rods of square cross-section. The Quarterly Journal of Mechanics and Applied Mathematics 28, 245–260. https://doi.org/10.1093/qjmam/28.2.245

Bancroft, D., 1941. The Velocity of Longitudinal Waves in Cylindrical Bars. Physical Review 59, 588–593. https://doi.org/10.1103/PhysRev.59.588

Chree, C., 1886. Longitudinal vibrations of a circular bar. The Quarterly Journal of Mechanics and Applied Mathematics 21, 287–298.

Guo, Y.B., Shim, V.P.W., Yeo, A.Y.L., 2010. Elastic wave and energy propagation in angled beams. Acta Mechanica 214, 79–94. https://doi.org/10.1007/s00707-010-0317-6

Kolsky, H., 1964. Stress waves in solids. Journal of Sound and Vibration 1, 88–110. https://doi.org/10.1016/0022-460X(64)90008-2

Lee, J.P., Kolsky, H., 1972. The Generation of Stress Pulses at the Junction of Two Noncollinear Rods. Journal of Applied Mechanics 39, 809–813. https://doi.org/10.1115/1.3422793

Maurel, A., Mercier, J.F., Félix, S., 2014. Propagation in waveguides with varying cross section and curvature: A new light on the role of supplementary modes in multi-modal methods. Proceedings of the Royal Society A: Mathematical, Physical and Engineering Sciences 470. https://doi.org/10.1098/rspa.2014.0008

Morse, R.W., 1948. Dispersion of Compressional Waves in Isotropic Rods of Rectangular Cross Section. The Journal of the Acoustical Society of America 20, 833–838. https://doi.org/10.1121/1.1906445

Pochhammer, L., 1876. Ueber die Fortpflanzungsgeschwindigkeiten kleiner Schwingungen in einem unbegrenzten isotropen Kreiscylinder. Journal für die reine und angewandte Mathematik (Crelles Journal) 1876, 324–336. https://doi.org/10.1515/crll.1876.81.324

Rayleigh, Lord, 1945. The Theory of Sound. Dover Publications, New York, NY, USA.

Rayleigh, Lord, 1888. On the Free Vibrations of an Infinite Plate of Homogeneous Isotropic Elastic Matter. Proceedings of the London Mathematical Society s1-20, 225–237. https://doi.org/10.1112/plms/s1-20.1.225

Subhash, G., Bavdekar, S., Leonard, R., Bagadion, M., Garcia-Suarez, J., Cheenady, A., Sheplak, M., Whittington, W., 2026. Concept Article: A Novel Compact Millipede Bar Waveguide for Propagation of Longitudinal Stress Waves. J. dynamic behavior mater. 12, 26–36. https://doi.org/10.1007/s40870-023-00399-2

Subhash, G., Garcia-Suarez, J., Cheenady, A., Bavdekar, S., Whittington, W., Molinari, J.-F., 2022. Stress wave propagation through a 180° bend junction in a square cross-sectional bar. Int. J. Eng. Sci. 180, 103748. https://doi.org/10.1016/j.ijengsci.2022.103748

Subhash, G., Leonard, R.Y., Whittington, W., Pending. Compact stress waveguide. US20230375448A1.

Subhash, G., Whittington, W., 2025. Compact mechanical waveguides for impact devices. US12409540B2.

Yong, K.H., Atkins, K.J., 1983. Generation of elastic stress waves at a T-junction of square rods. Journal of Sound and Vibration 88, 431–436. https://doi.org/10.1016/0022-460X(83)90646-6

Yong, K.H., Atkins, K.J., 1982. Generation of elastic stress waves at a corner junction of square rods. Journal of Sound and Vibration 84, 431–441. https://doi.org/10.1016/0022-460X(82)90488-6